Hindawi
Advances in Meteorology
Volume 2022, Article ID 1030330, 15 pages
https://doi.org/10.1155/2022/1030330

Research Article

Wavelet Analysis of the Interconnection between Atmospheric Aerosol Types and Direct Irradiation over Cameroon

Yaulande Alotse Douanla,[1] **Ossénatou Mamadou**,[1,2] **André Dembélé**,[3] **Djidjoho Renaud Roméo Koukoui**,[1] **Fifamè Edwige Akpoly**,[4] **and André Lenouo**[5]

[1]*Institute of Mathematics and Physics (IMSP), Dangbo, Benin*
[2]*Laboratoire de Physique Du Rayonnement (LPR/FAST), University of Abomey-Calavi, Godomey, Benin*
[3]*Department of Mathematics and Informatics, Faculty of Sciences and Technics (FST), Bamako, Mali*
[4]*African Institute for Mathematical Sciences (AIMS), Cape Town, Senegal*
[5]*Laboratory of Physics, University of Douala, Douala, Cameroon*

Correspondence should be addressed to Yaulande Alotse Douanla; yaulande.douanla@imsp-uac.org

Received 18 April 2022; Revised 27 July 2022; Accepted 3 August 2022; Published 5 September 2022

Academic Editor: Pedro Salvador

The comparative analysis of the intra- and interannual dynamics between the Direct Normal Irradiation (DNI) under clear sky conditions and five aerosol types (Dust, Sea Salt, Black Carbon, Organic Carbon, and Sulfate) is the purpose of this study. To achieve this aim, we used fifteen-year DNI and aerosols data downloaded at 3-hour time intervals in nine defined zones throughout Cameroon. The wavelet transform is a powerful tool for studying local variability of amplitudes in a temporal dataset and constitutes our principal tool. The results show unequal distribution of aerosol types according to zones, but the Desert Dusts (DU) and Organic Carbon (OM) aerosols have been found as dominant particles in the studied region. The wavelet coherence analysis between DNI and each aerosol type reveals three bands of periodicity: ~4-month band, 8–16-month band, and sometimes after-32-month band, with the most important frequency at 8–16-month band period. However, the intensity of coherence across bands varies with respect to aerosol type as well as each of the nine climate zones. A significant anticorrelation relationship was obtained between DNI and each type of aerosol, emphasizing that the presence of such atmospheric particles could dampen the renewable energy utilized by power systems. Also, the analysis shows that scattering aerosols such as Sulfate and Sea Salt (SU and SS, respectively) lead DNI in phase while absorbing aerosols such as Organic Carbon, Black Carbon, and Dust (OM, BC, and DU, respectively) give phase lag with DNI.

1. Introduction

Atmospheric aerosols are fine particles (solid, liquid, or gaseous) in suspension in the atmosphere, emitted by either natural or anthropogenic sources [1]. Their spatiotemporal distribution is highly variable, depending mainly on geographical features and meteorological conditions (wind, temperature, precipitation, radiation, etc.). The latter can in turn influence aerosol particles before their removal from the atmosphere. These particles are also known as one of the main components in the atmosphere that significantly contribute to regional and global climate change [2] and hydrological and biogeochemical cycles [3]. From various sources, aerosol particles play a key role through complex interactions, in participating in the atmospheric radiative transfer either directly by scattering and absorbing solar radiation or indirectly by changing the optical properties and lifetime of clouds [1, 4, 5]. In addition, their increase may interfere with the earth's energy balance, causing the climate system to either gain or lose energy [2].

Several studies show that anthropogenic aerosols can modify radiative forcing [6, 7], monsoon dynamics [5, 8, 9], and diurnal precipitation cycle [10, 11]. In Central Africa, Komkoua et al. [10] and Komkoua et al. [11] studied the

impact of anthropogenic aerosols on climate variability and the hydrological cycle by undertaking experimental simulations with RegCM4.4 model. They found that anthropogenic aerosols might reduce shortwave radiation by up to 6 W/m^2 during the dry season over the 0–10°N band. This impact resulting in a surface cooling of more than 0.4°C (triggered by local aerosols of Organic and Black Carbon) is at the origin of the decrease of dry season precipitation in Southern Africa during the last century [10–12]. According to [13], the amount of reflected radiation by Sulfate aerosols depends nonlinearly on relative humidity. However, because of the absorbing properties of Black Carbon and carbonaceous aerosols, these two types of aerosols can decrease the amount of reflected radiation at the top of the atmosphere [13]. Regarding the natural aerosols, Dust impacts on clouds and precipitations are well known to be important. However, their effects nowadays remain highly dependent on the cloud types and meteorological conditions [14]. A sensitivity analysis of an increase of Sea Salt aerosols emissions with temperature done in [15] suggests that their increase may even reduce climate sensitivity. The remarkable evidence emerging from these worldwide obtained results shows how these different types of aerosols affect climate at different scales and in various ways.

Direct Normal Irradiation (DNI) is the amount of solar radiation received per unit area by an area perpendicular to the sun's rays [16]. This is of particular interest to implement renewable energy such as concentrated solar thermal electricity systems [17]. However, the knowledge of the long-term spatiotemporal distribution of aerosols and their relationship with DNI in Central Africa, especially over Cameroon, remains limited. To overcome this gap, recently based on a machine learning approach (Extreme Gradient Boosting), we proposed a prediction model of DNI using some meteorological variables and different aerosol types over Cameroon [18]. The interpretation of the model outputs using Shapley's value showed that, in the whole study area, DNI is most influenced by Desert Dust (DU), Organic Carbon (OM), and Sulfate aerosols (SU) [18]. However, it is well known that, in addition to the weather conditions, the available energy also depends on the type and quantity of aerosols that are present. The aim of this paper is to analyze in nine regions of Cameroon (a) the influence of aerosol types on DNI and (b) the spatiotemporal aspect of this interaction by using wavelet transform.

Formalized in a rigorous mathematical framework, the wavelet transform is a statistical method allowing the analysis of nonstationary data in the time-frequency domain [19–22]. It has been previously used to distinguish frequency bands where one or two time series are associated. Recently, several examples of wavelet analysis applications on various meteorological data [23–28] and aerosol time series [29–31] have been studied: in particular, as a method for detecting the short- and long-term periodicity of radiation data [32–37].

Herein, the continuous wavelet transform (CWT) suitable for continuous variables is used. Continuous wavelet transformations and wavelet coherence were implemented to assess the relationship between meteorological variables and DNI at different periodicities. The aim is to identify seasonal and interannual scales of variability and time-frequency dependencies in different areas throughout Cameroon. Emphasis is put on the exploitation of data of five aerosol species, namely, Desert Dust, Sea Salt, Black Carbon, Organic Carbon, and Sulfates, and Direct Normal Irradiation from 2005 to 2019. This paper is organized as follows: we present the materials and methods guiding this study (Section 2). We give an overview of the spatiotemporal distributions of the five aerosol types as well as their consistency with direct wavelet irradiation, to be checked in Section 3. Finally, we discuss our results and give a conclusion afterwards.

2. Materials and Methods

2.1. Study Area and Its Climate. Cameroon is a country in West-Central Africa located between latitudes 1.6°N–13°N and longitudes 8°E–17°E. Cameroon encompasses approximately 475440 km^2 (Figure 1). The country is bordered by Nigeria and the Atlantic Ocean to the West, Chad to the North, Central African Republic to the East, and Gabon, Equatorial Guinea, and the Democratic Republic of Congo (DRC) to the South. It has several climate types with contrasting physical and biogeographic characteristics [38]. From the north to the south of the country, the climate is dry and Sudano-Sahelian type with total annual rainfall of about 500 mm (from Ngaoundéré to the far north) to a humid equatorial climate ranging from a bi- or unimodal regime for rainfall (total annual rainfall of 3000 mm) in the southwestern part of the Cameroon plateau [39]. The center is the Guinean savanna zone, while in the west the center is the high mountain zone. The south part is dominated by forest area which is associated with a large hydrographic network and a dry climate. The mean temperature ranges from 22°C to 29°C, increasing from south to north and from the coast to the hinterland [38]. In the mountains area (Adamawa North West and Adamawa West), air temperature varies with altitude from 24.4 to 25°C [40].

As the country is endowed with climatic diversity that varies from North to South and from East to West, choosing various subzones encompassing this diversity is imperative to ensure optimal representativity of its climate. To do that, compared to other available approaches [41–44] we choose the K-means clustering because of the efficiency flexibility in its implementation [45]. This clustering algorithm consists in grouping observations into K clusters in which each observation belongs to the cluster with the nearest mean [45]. However, the determination of the optimal value K of the number of clusters is very hard. To remedy this, two algorithms (Silhouette and Elbow [46–48]) are used to find K. Following this classification, a total of nine (9) representative clusters were extracted. More details can be found in [18].

2.2. Data. Data from two databases are used to perform analyses in this study. These are CAMS-Radiation (Copernicus Atmosphere Monitoring Service) service

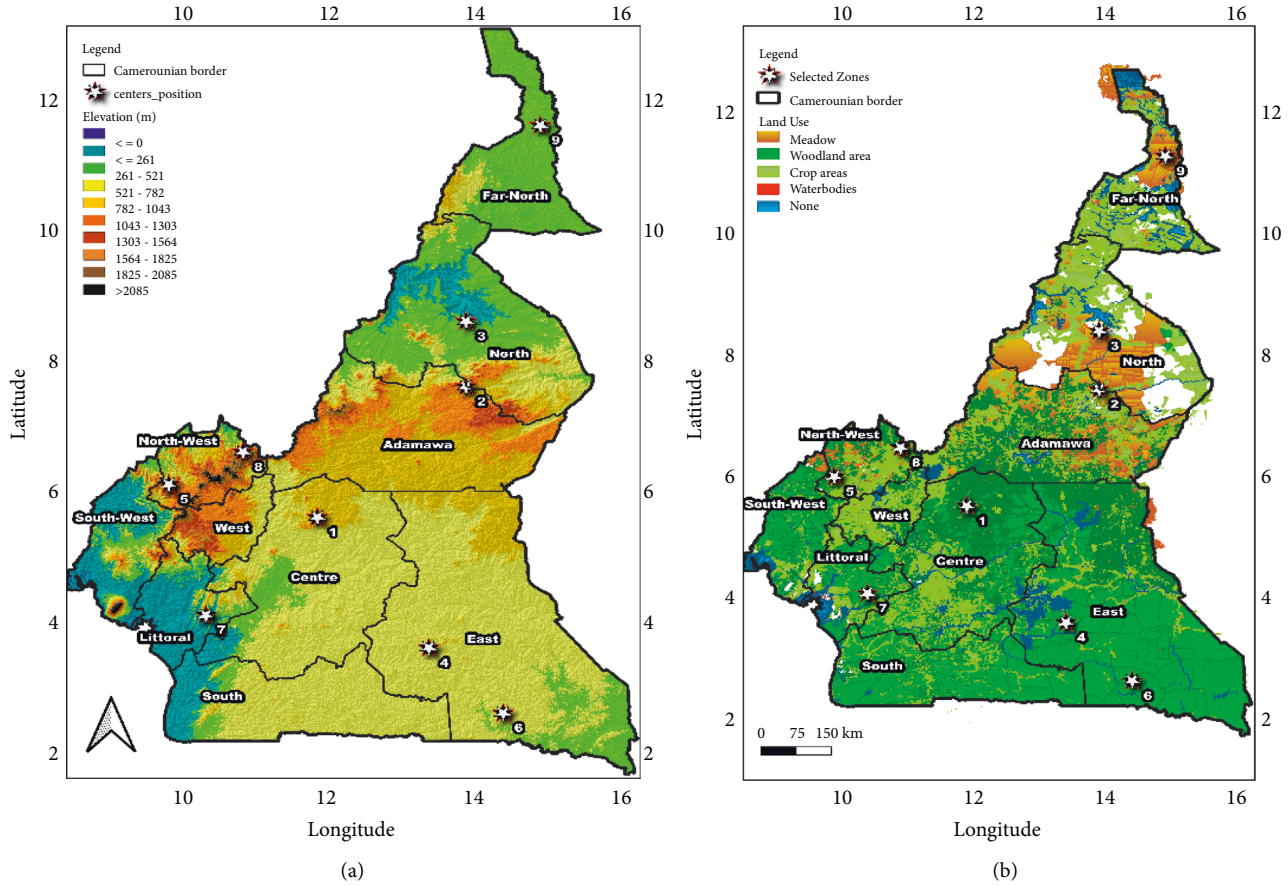

Figure 1: Topography of the study area (left) and land use map (right) using OpenStreetMap data (https://download.geofabrik.de/africa/cameroon-latest-free.shp.zip). The stars identified the target zones found with the *K*-mean classification method.

(https://www.soda-pro.com/web-services/radiation/cams-radiation-service) with a spatial resolution of $0.58^{\circ} \times 0.6258^{\circ}$ and CAMS-AOD (https://www.soda-pro.com/web-services/atmosphere/cams-aod) [49, 50]. The Direct Normal Irradiation data under clear sky conditions (BNI.clear.sky), namely, DNI, has been downloaded from CAMS-Radiation service at a 3-hour step. The Aerosols Optical Depth (AOD) at 550 nm of five aerosols species, Sea Salts (SS), Black Carbon (BC), Organic Carbon (OM), Desert Dust (DU), and sulphate aerosols (SU), was retrieved from the CAMS-AOD database at 3-hour time step. Data is downloaded for the period 2005–2019 over the nine areas identified by Silhouette, Elbow, and *K*-means methods (see Figure 1). Data are transformed to monthly data by taking the arithmetic average in the subsequent analysis.

Regarding the temporal evolution of AOD types (Figure 2), a significant change (increase or decrease) is noticed in all areas. In fact, within the framework of the European projects, namely, GMES (Global Monitoring for Environment and Security), MACC (Monitoring Atmospheric Composition and Climate), and CAMS, the ECMWF (European Center for Medium-Range Weather Forecasts) laboratory has developed a weather forecasting model named "CAMS Global Forecast" or "CAMS IFS Forecast" (https://confluence.ecmwf.int/display/CKB/CAMS%3A + Global + atmospheric + composition + forecast + data + documentation). The aerosol data that SoDa (CAMS-AOD) distributes is part of the output of this model. This model is updated about once a year, not retroactively. ECMWF does not ensure continuity during updates, so small jumps in the aerosol quantities estimated by the model can happen. For this purpose, the 2004–2012 data are different because they come from a version of IFS named "CAMS IFS Forecast" and the one distributed after 1/1/2013 comes from "MACC Reanalysis" (https://confluence.ecmwf.int/pages/viewpage.action?pageId=81010554). These are reanalyses, that is, a modified version of IFS where measurements of temperature, wind, pressure, etc. throughout the whole world have been ingested. This improves the accuracy of the model.

2.3. Wavelet Analysis. Several types of wavelet transforms exist in the literature which can be categorized into discrete or continuous [22]. In this study, we used continuous wavelet transform (CWT) because of its ability for scale analysis and adapting for analyzing localized intermittent oscillations in aerosols and DNI data.

2.4. Continuous Wavelet Transform (CWT). Continuous Wavelet Transform analyzes the variability in the studied signal (univariate mode) and measures the correlation between two signals (bivariate mode) according to the time and

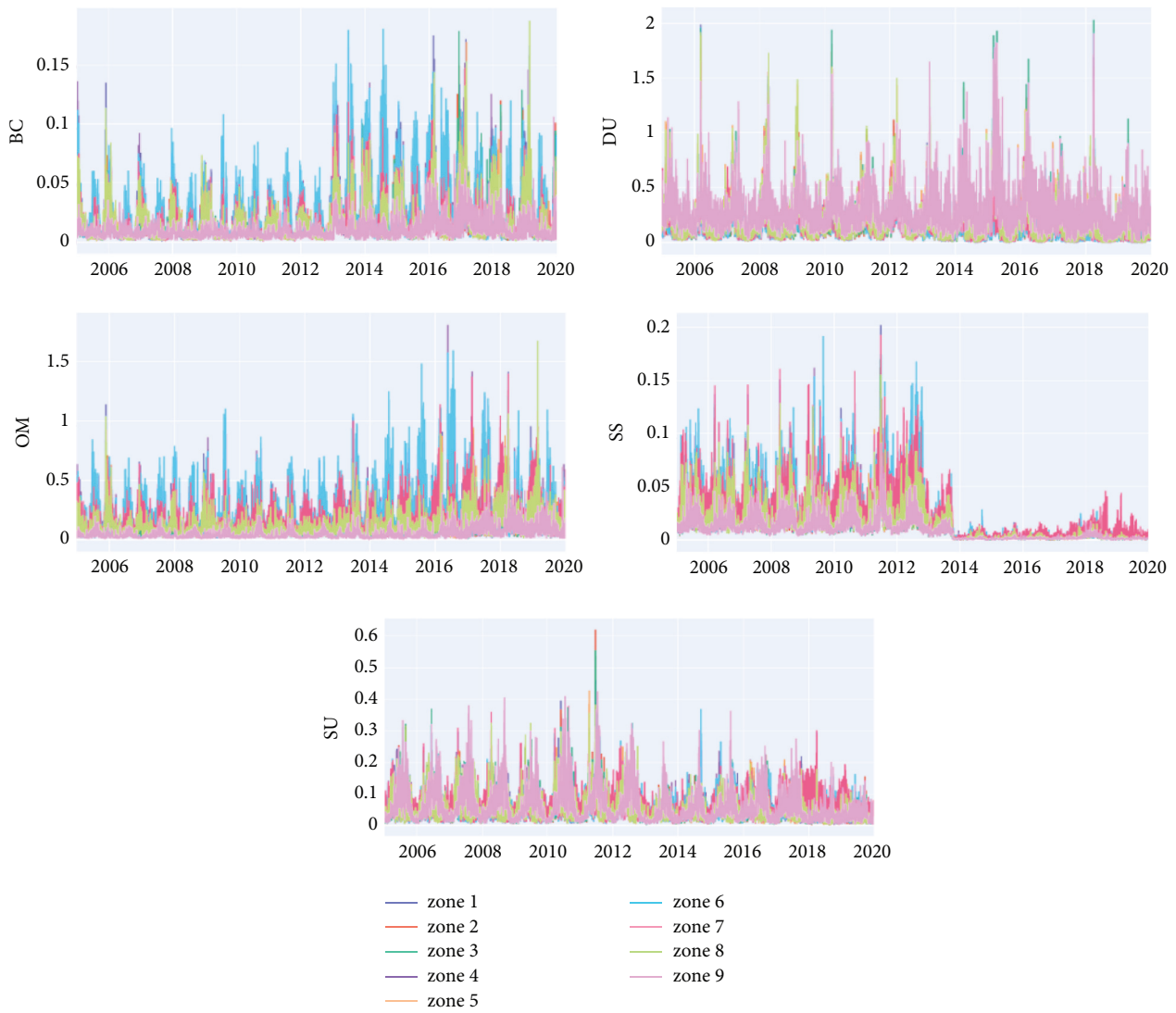

Figure 2: Temporal variability of monthly mean of aerosols over studied zones.

scale. For the analysis of variability, the issue is to determine whether these variations are cyclical or random. The wavelet transform of a sequence of observations $x(t)$ is the convolution of $x(t)$ by analyzing the wavelet function $\Psi_{a,b}(t)$:

$$W_x(a,b) = \int_{-\infty}^{+\infty} x(t)\Psi_{a,b}^*(t)\mathrm{d}t, \tag{1}$$

where $\Psi_{a,b}^*(t)$ is the conjugate of $\Psi_{a,b}(t)$ [51, 52]. Many wavelet functions are available in the literature. In this study, Morlet's function [53, 54] is used because of its ability to detect specific periodic behaviors in a signal [55]. In addition, it consists of both real and imaginary parts that enable investigating a signal's coherence and phase angle [22, 33, 35]. This function is given by

$$\Psi(t) = \pi^{-1/4} e^{i\omega_0 t} e^{-t^2/4}, \tag{2}$$

where ω_0 is the dimensionless frequency taken to be equal to 6 in order to fulfill the admissibility criterion [22]. From (2), Jean Morlet constructed $\Psi_{a,b}(t)$ such that

$$\Psi_{a,b}(t) = \frac{1}{\sqrt{2}}\Psi\left(\frac{t-b}{a}\right), \tag{3}$$

where $(a > 0)$ and $(b \in R)$ are, respectively, the scale and translation parameters. For given values of (a, b), $W_x(a,b)$ becomes a wavelet coefficient. The implementation of the continuous wavelet transform involves steps which are outlined as follows [56]:

(1) Selection of the mother wavelet $\Psi(t)$

(2) Initialization of a and b values

(3) Placing the mother wavelet $\Psi(t)$ at the beginning of an arbitrary signal $x(t)$ at the point corresponding to $t = 0$

(4) Determining $W_x(a,b)$

(5) Progressively translating the mother wavelet $\Psi(t)$ to the right of a Step b, i.e., to a position $t = b$

(6) Resuming Step 4, till the signal is covered entirely by the mother wavelet

(7) Increasing the value of a

(8) Resuming Step 3, till the desired value of a is attained

However, for scale values which can be written as $a = 2^j$ [54], the continuous wavelet transform (CWT) is equivalent to the discrete wavelet transform with the coefficients described in the following equation [55]:

$$W_x(a,b) = \left(\frac{\delta t}{a}\right)^{1/2} \sum_{n=0}^{N-1} x_n \Psi^*_{a,b}\left(\frac{n\delta t - b}{a}\right), \tag{4}$$

where a is given by [22, 55]

$$a_j = a_0 2^{j\delta j};\ j = 0, 1, 2, \ldots, J, \tag{5}$$

with

$$J = \frac{1}{\delta j}\log_2\left(\frac{N\delta t}{a_0}\right), \qquad a_0 = 2\delta t. \tag{6}$$

Herein, monthly data have been used for the computation. Thus, the parameter values become $N = 181$, $\delta t = 1$ month, $\delta j = 0.0833$, and then, $J = 59$.

2.5. Wavelet Coherence (WC) and Phase Function. Coherence analysis, cospectral power, and wavelet phase coherence are often used to identify the degree of correlation between two signals. The wavelet coherence expressed in (7) enables highlighting relations of influence between two signals at different frequencies (scales) as a function of time [36, 37, 53, 57]. Its values range between 0 and 1.

$$C_{xy}(a,b) = \frac{Sa^{-1}W_{xy}(a,b)}{\sqrt{S\left(a^{-1}\left|W_x(a,b)\right|^2\right)S\left(a^{-1}\left|W_y(a,b)\right|^2\right)}}, \tag{7}$$

with

$$W_{xy}(a,b) = W_x(a,b)W^*_y(a,b), \tag{8}$$

and $S = S_a(S_t(W_{xy}(a,b)))$is a smoothing factor [55]. Phases are obtained from the calculated values of the imaginary and real parts of the cross spectrum W_{xy} expressed in (8) and are formulated as follows:

$$\theta_{xy}(a,b) = \frac{\mathrm{Im}\left(W_{xy}(a,b)\right)}{\mathrm{Re}\left(W_{xy}(a,b)\right)}, \tag{9}$$

with $\theta_{xy} \in [-\pi, +\pi]$ in radians.

For a phase angle of 0, that is, when the series are in phase, the arrows on the scalogram point right, implying that the two series have a high coherence, while for a phase angle of 180 (antiphase), the arrows point left [58]. For 90 and 270, the arrows point vertically downwards and vertically upwards, respectively.

2.6. Significance of Correlation. To statistically assess the correlation between two variables, one can also calculate the average wavelet coherence (AWC) and the percentage of significant coherence (PASC) [59, 60]. The AWC is the average value of wavelet coherence produced over all scales, while PASC is the percentage of significant values over the total number of power values produced in the WC. A significant power is one where the ratio of WC values over the significance level is greater than 1. In this study, a higher AWC with larger PASC means that more variation in DNI can be explained by that specific case of connection.

3. Results

3.1. Intra-Annual Aerosols Distributions. Figure 3 displays the monthly average of the five types of aerosols investigated over the period 2005–2019: Black Carbon (BC), Desert Dust (DU), Organic Carbon (OM), Sea Salts (SS), and Sulfates (SU). The aerosol distributions are observed seasonally.

DU and OM are dominant throughout the year in zones 1, 2, 3, 5, and 9.

However, in zones 4, 6, and 7, the OM content is a bit higher than that of the other aerosol types. In contrast to OM dynamics, we noticed that BC is one of the lowest over the studied zones. Moreover, it can be noticed over the nine zones that DU increased from September (Figure 3) corresponding to the dry month to reaching their maximum in March. The peak of Dust obtained in March can indeed be explained by sandstorms which occur at this time of year [61]. Regarding the Organic Carbon aerosol, two cycles appear in its seasonality: higher values from November to March and from June to August, followed by lower values in the remaining months. This tendency has been observed in all zones and can be attributed probably to the agriculture cycle.

3.2. Continuous Wavelet Power Spectrum (CWS) of Aerosol Types. The wavelet power spectrum ($|W_x(a,b)|^2$) of each aerosol type (shown in Figures 4 and 5) quantifies the amount of signal variability explained by the wavelet at each time step and scale. In the following, we describe the CWS of the monthly average of DNI and each aerosol type.

In Figure 5, the CWS power is more concentrated within the 8–16-month band, showing that DNI has a strong annual signal in all studied zones except for zones 4 and 6 where a seasonal variation (4–8-month band) is found:

> For the Black Carbon aerosol (BC), we observe different periodicity according to the zones starting in 2013 (Figure 4). In zones 4 and 6, for example, which are mainly forest areas (Figure 1), the frequency of variability is 6 months (i.e., seasonal variability), while for zones 9, 2, and 3 dominated by grassland, it is 12 months, hence an interannual variability. For the remaining zones, the two abovementioned variability bands are observed (seasonal and interannual variability).

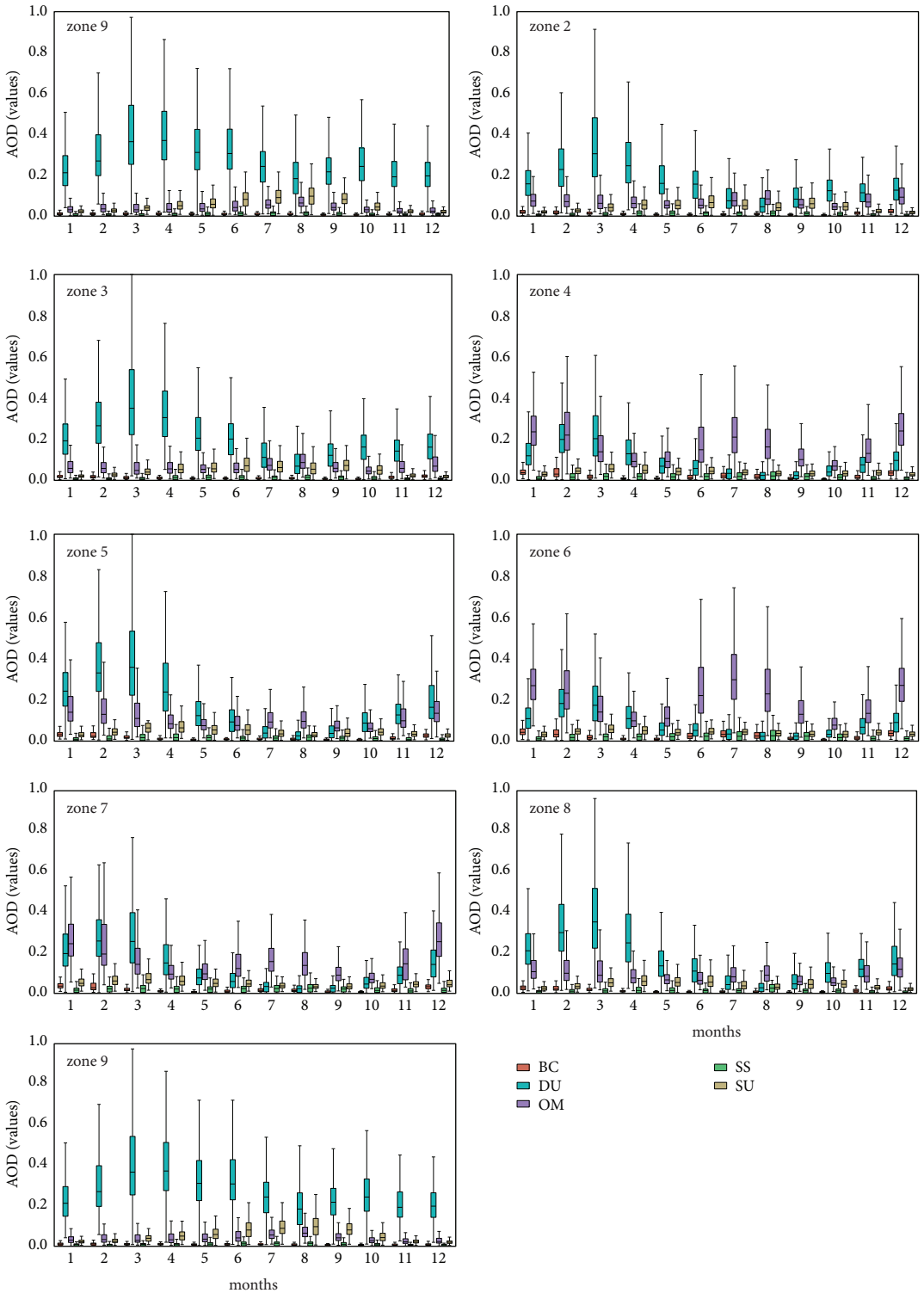

Figure 3: Intra-annual variability of aerosol optical thicknesses.

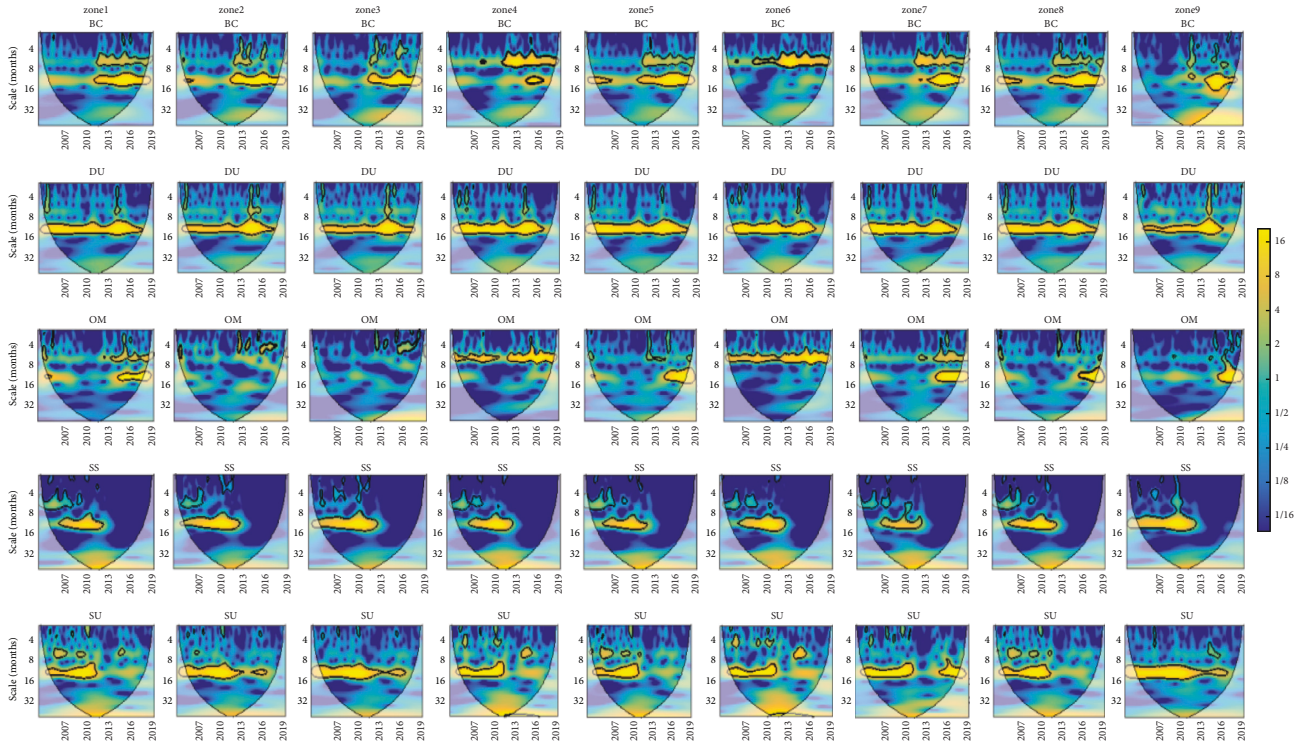

Figure 4: Continuous Morlet wavelet spectrum (CWS) of the five types of aerosols over the 9 selected zones on a monthly scale during 2005–2019. The thick black contours are the 95% confidence level of local power relative (significant periodicities are enclosed in that thick black contour line). The black line is the cone of influence beyond which the energy is affected by the zero-padding effect.

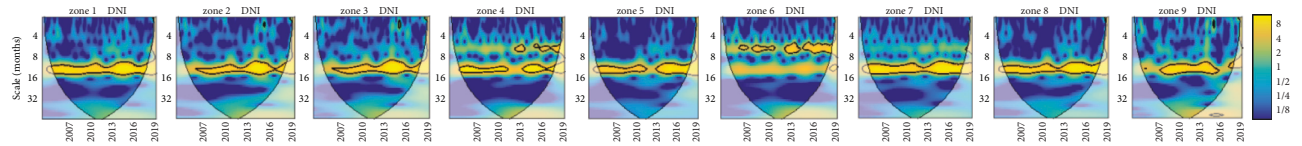

Figure 5: Continuous Morlet wavelet spectrum (CWS) of DNI over the 9 selected zones on a monthly scale during 2005–2019.

For the Desert Dust aerosol (DU), contrary to the previous case (BC), a single frequency of variability is observed here at 12 months in all zones and over the entire study period (2005–2019), suggesting an interannual variation (Figure 4).

In the case of the Organic Carbon aerosol (OM), in zones 4 and 6 (dominated by forest areas), a 6-month periodicity frequency appears indicating a seasonal variability. As for the other zones (except for zones 2 and 3 which are the grassland areas), two frequency bands (6 and 12 months) appear after 2013 (Figure 4).

Regarding the Sea Salt aerosol (SS), before 2013, a significant interannual variability (12 months) is observed in all areas and after 2013, no variability appears (Figure 4).

For the Sulfate aerosol (SU), a variability band appears at 12 months in zones 2, 3, and 9 although after 2013 a slight decrease in wavelet intensity is noted. For the rest of the zones, before 2013 also, the variability is also at the frequency (12 months) but after 2013 the decreasing is more significant than in the previous zones (Figure 4).

3.3. Relationship between Aerosol Types and Direct Energy. The wavelet coherence analysis between five aerosol types (SU, SS, OM, BC, and DU) and DNI (Direct Normal Irradiation under clear sky conditions) of the nine climate zones involved in this study is presented below. Figures 6–10 show the normalized power of the wavelet coherence spectra calculated from the monthly time series for the period spanning from 2005 to 2019. In those figures, the *u*-shape boundary is referred to as the cone of influence (COI). The inner space of this cone defines the region of the spectrum to be considered in the analysis. It actually denotes the areas where the effects of the edge occur throughout the time series [22, 33, 62]. The thick black contours are the regions that are significant at the 95% confidence level [22, 33, 58, 62].

Overall, from the wavelet coherence between each aerosol and the DNI, various frequencies depending on the aerosol types and areas are noticed (Figures 6–10). To better

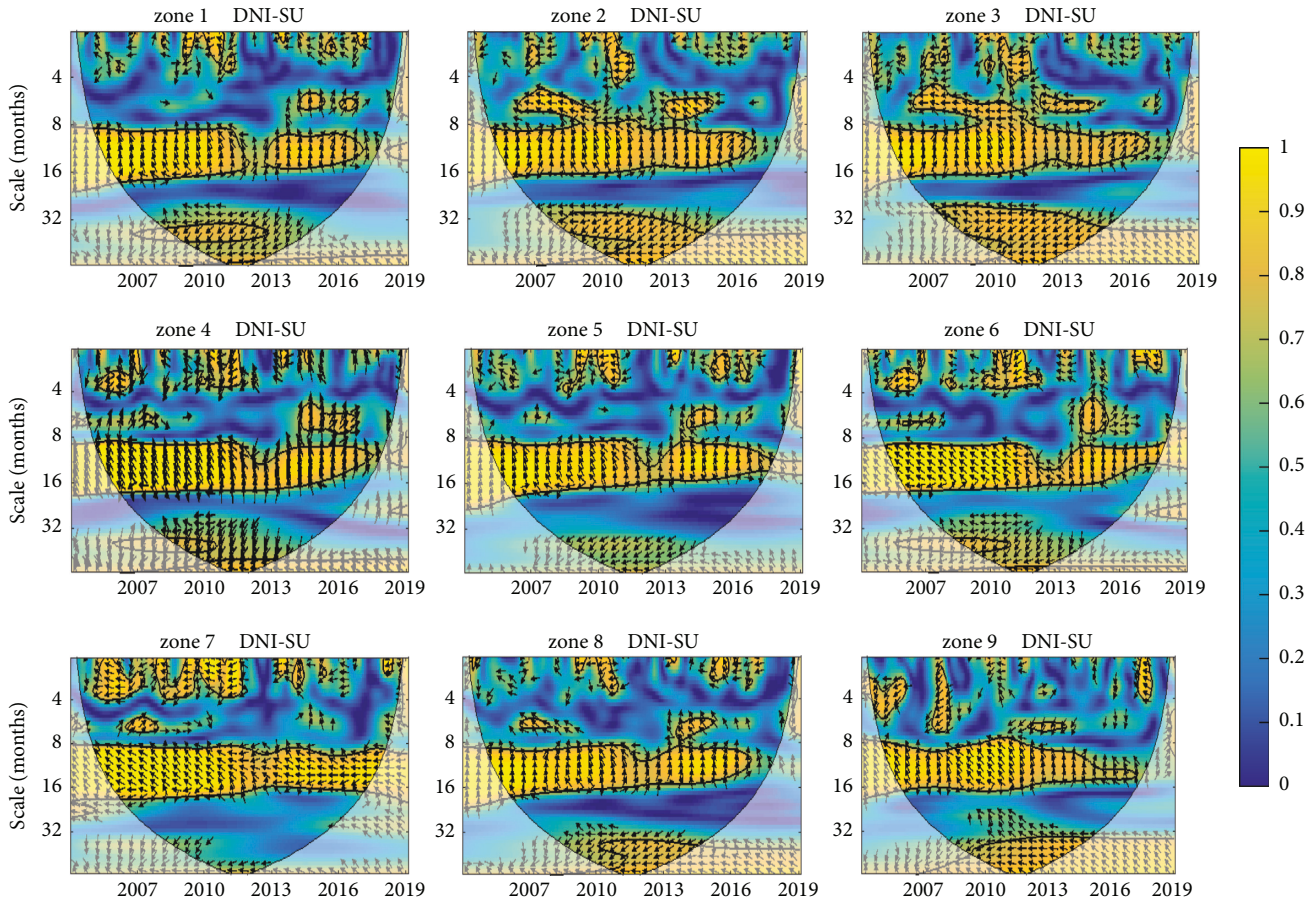

Figure 6: Wavelet coherence between the monthly average of DNI and SU time series (2005–2019). Areas of statistical significance are circled in black; the area outside the cone of influence has no statistical significance. SU and DNI in phase if arrows are pointed to right and out of phase otherwise.

understand their influence on the DNI, the average wavelet coherence power (AWC) and percentage of significant coherence (PASC) are calculated over all scales to measure the relative dominance of individual aerosols on the DNI. Arrows are also shown to illustrate the phase dependence. The regions where the two parameters are moving in phase are represented by arrows directed to the right, and in the opposite phase if arrows are directed to the left, and the aerosol or irradiation variable is leading (or lagging) if arrows are directed downward (or upward), respectively [58].

3.4. Sulfate Aerosols (SU). The relationship between Sulfate aerosols and Direct Normal Irradiation is displayed in (Figure 6). In all areas, SU is significantly and negatively correlated with direct irradiation. The regions with the coefficient of correlation exceeding 0.8 (yellow color) appear at 4-month band, within 8–16-month band, and after-32-month band whereas the 8–16-month band is the most important one (Figure 6). Additionally, arrows at those frequencies point to the left and are oriented upward, suggesting that SU and DNI are anticorrelated in all zones with SU in phase advance on DNI. Referring to AWC and PASC, the most important values are recorded in zone 3 with AWC and PASC equal to 56 and 33.72, respectively (Table 1), and lower values are recorded in zone 5 with AWC and PASC equal to 0.48 and 20.80, respectively (see Table 1).

3.5. Sea Salt Aerosols (SS). Figure 8 shows the wavelet coherence between the Sea Salt aerosols and DNI. The regions of the spectrum in which the correlation coefficient is greater than 0.8 are mainly located between 8–16-month and after-32-month bands. The wavelet energy distribution is discontinuous before 8 months and more concentrated in the remaining bands. However, over all areas, the correlation tends to disappear after 2013 in the 8–16-month band. As for phases, in all bands, arrows are pointed to the left, suggesting an out of phase (anticorrelation). In addition, they are oriented upward, implying that SS leads DNI.

3.6. Organic Aerosols (OM). Regarding organic aerosols (Figure 9), they are also anticorrelated with DNI in different bands. But, in zones 2 and 3, organic aerosols and Direct Irradiation are weakly correlated as indicated by their AWC and PASC values (Table 1). In zones 4 and 6 (forest areas) in which OM are the most dominating aerosols (Figure 3) on a seasonal scale, since the dominant correlation band is within

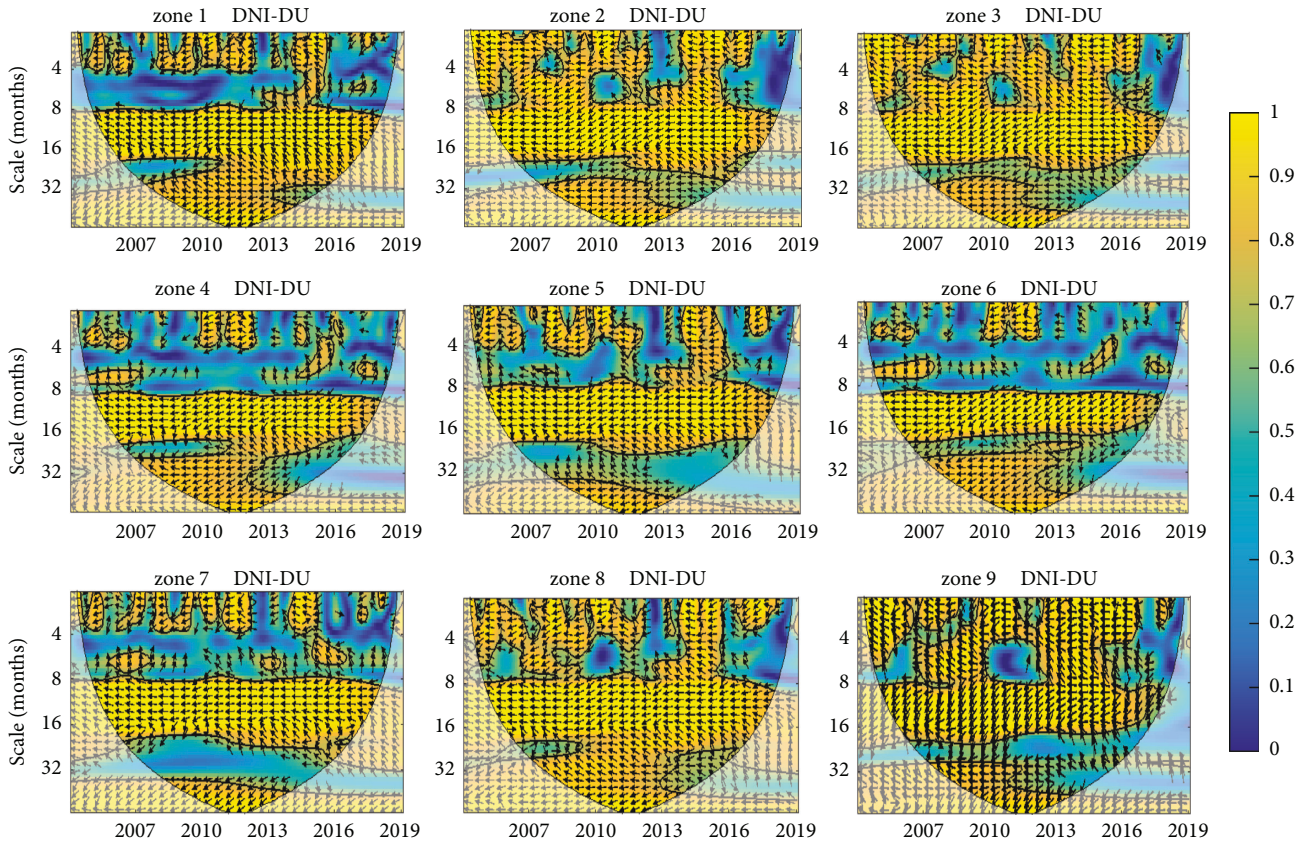

Figure 7: Wavelet coherence between the monthly average of DNI and DU time series (2005–2019). Areas of statistical significance are circled in black; the area outside the cone of influence has no statistical significance. The relative phase dependence is indicated by arrows (antiphase as oriented toward the left, and DNI in advance of phase to DU as arrows pointed downward).

Table 1: Average wavelet coherence (AWC) and the percentage of the significant power (PASC) values for wavelet coherence analysis of all the 9 zones.

	Zone 9		Zone 3		Zone 2	
Combinations	AWC	PASC (%)	AWC	PASC (%)	AWC	PASC (%)
DNI-BC	0.46	19.06	0.49	23.94	0.49	32.70
DNI-DU	0.73	61.16	0.77	68.84	0.76	61.92
DNI-OM	0.45	20.30	0.43	18.48	0.44	34.62
DNI-SS	0.53	40.17	0.55	41.64	0.56	40.86
DNI-SU	0.52	29.87	0.56	33.72	0.54	23.23
	Zone 5		*Zone 8*		*Zone 7*	
DNI-BC	0.55	31.83	0.53	28.50	0.61	45.29
DNI-DU	0.70	53.18	0.78	71.04	0.70	53.12
DNI-OM	0.53	31.68	0.49	25.67	0.64	50.98
DNI-SS	0.57	39.23	0.57	41.95	0.53	33.10
DNI-SU	0.48	20.80	0.49	27.62	0.54	28.43
	Zone 1		*Zone 6*		*Zone 4*	
DNI-BC	0.58	32.70	0.57	37.52	0.61	31.83
DNI-DU	0.72	61.92	0.63	43.79	0.65	53.18
DNI-OM	0.59	34.62	0.55	37.43	0.56	31.68
DNI-SS	0.57	40.86	0.52	33.66	0.54	39.23
DNI-SU	0.50	23.23	0.53	27.66	0.53	20.80

4–8 months, the correlation is too high (Table 1). Finally, the correlation between DNI and OM in zones 1 and 7 is greater than 0.50.

3.7. Black Carbon Aerosols (BC). For BC and DNI (Figure 10), they are anticorrelated but with phase advance irradiation as arrows are oriented to the left and pointing

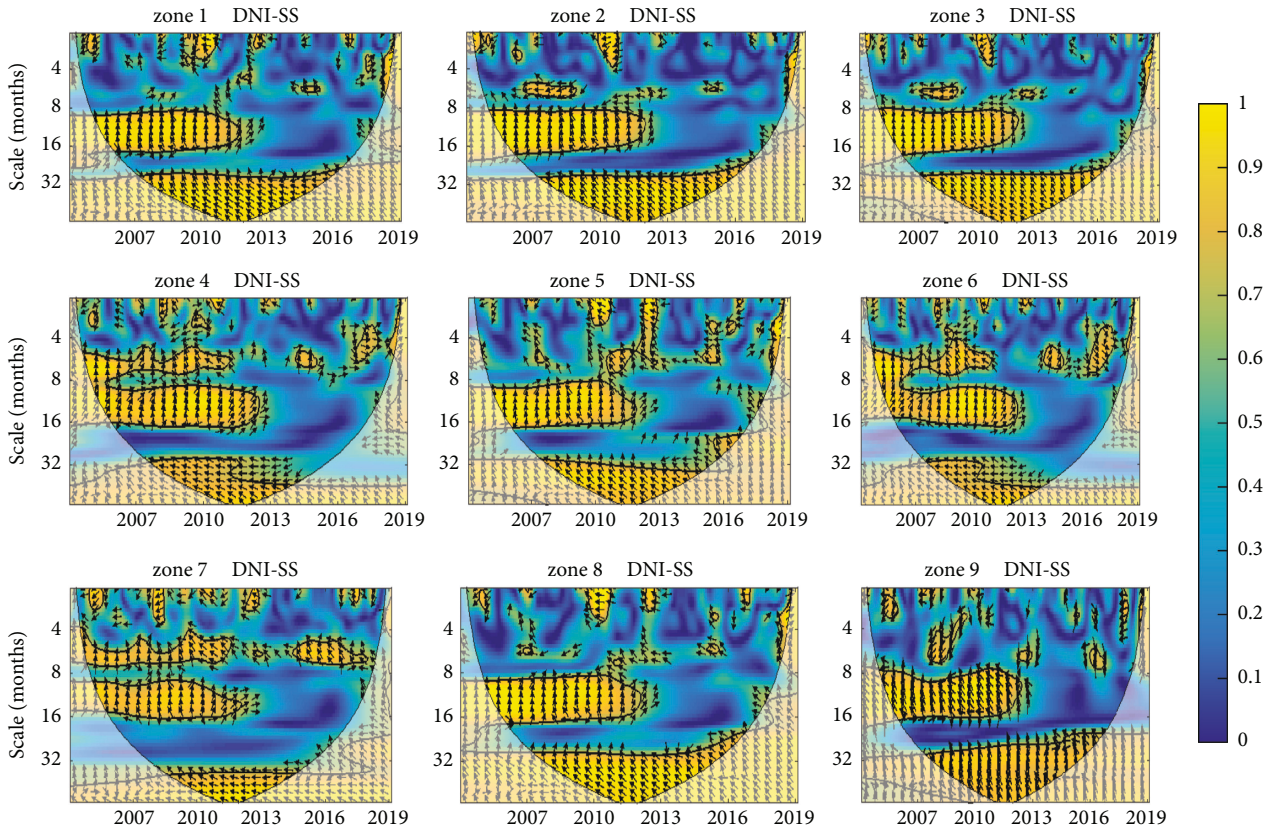

Figure 8: Wavelet coherence between the monthly average of DNI and SS time series (2005–2019). Areas of statistical significance are circled in black; the area outside the cone of influence has no statistical significance. The relative phase dependence is indicated by arrows (antiphase as oriented toward the left, and DNI in advance of phase to SS as arrows pointed upward).

downward. The correlation is significant before 18 months where the most important frequency is within 8–18 months as in all zones, and that band is continuous all over the study period except for zones 6 and 9. When looking at AWC and PASC, low values are recorded in zones 9, 2, and 3 (Table 1) and the highest AWC and PASC are recorded in zone 7 (0.61 and 45.29, resp.).

3.8. Desert Dust Aerosols (DU). Finally, the relationship between DU aerosols and DNI is presented in Figure 7. DU is negatively correlated with DNI leading DU. Regions with a wavelet correlation coefficient greater than 0.8 occupy about 2/3 of the figure in almost all regions. However, the 8–18-month band is over the entire study period. Based on AWC and PASC, DU and DNI are less correlated in zones 4 and 6.

4. Discussion

From the climatology study (Figure 3), we found that the quantity of each type of aerosol within a region is very unevenly distributed and that the quantity of each type varies with the months. During the dry seasons (December to February or March), the optical thickness of aerosols is high no matter the region and low during other seasons, except for organic aerosols (OM), for which two seasons of significant variability are distinguishable. The high optical thickness values during the dry seasons are due to the absence of rain, which is the main agent of atmospheric leaching [63]. The seasonality of organic aerosols in the study area is such that the periods of low values of OM (April, May, August, and September) correspond to the periods after sowing and the remaining months where high values of OM were obtained fit with the green period (dense vegetation). As for Dust aerosols, their values are high in all regions recorded between February, March, and April, which correspond to the period of sandstorms in northern Cameroon. Knowing that winds favor aerosol transport, Dust particles coming from the North under the effect of the storm can be spread over the whole territory under the influence of the wind.

In addition, the spatiotemporal analysis of aerosols shows a weak or even negligible presence of Black Carbon aerosols in all areas (Figure 3). The wavelet coherence analysis, on the other hand, reveals relevant information about them. Indeed, if we were to stick to the results of Figure 3, we would consider Black Carbon aerosols negligible with respect to Dust aerosols and Organic Carbons. However, wavelet analysis reveals that, in an area where OM is strongly correlated with DNI such as in zone 7 (a woodland zone predominate by oil palm plantations) [64, 65] where the AWC and PASC values of OM particles are the highest, BC is also highly correlated with DNI; the reciprocal can be observed in zones 2, 3, and 9, where OM is

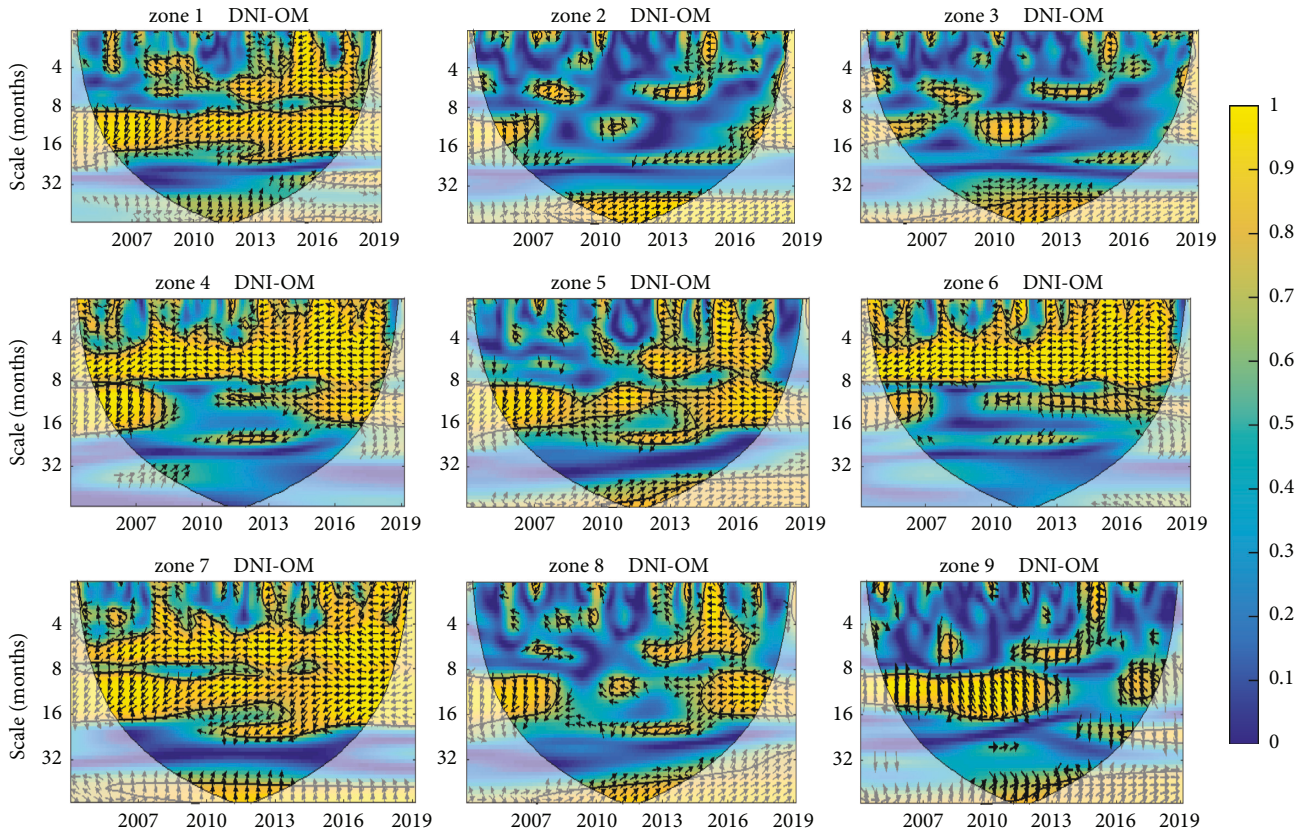

Figure 9: Wavelet coherence between the monthly average of DNI and OM time series (2005–2019). Areas of statistical significance are circled in black; the area outside the cone of influence has no statistical significance. The relative phase dependence is indicated by arrows (antiphase as oriented toward the left, and DNI in advance of phase to OM as arrows pointed downward).

weakly correlated with DNI and so is BC. This result can be justified by the strong correlation (0.8) between BC and OM (Figure 11). This result is in agreement with the one presented in Figure 11 where the highest correlation (0.8) is between BC and OM. However, this correlation holds in one direction (the greater the OM quantity, the stronger the effect of BC on DNI according to the environmental characteristics). Indeed, according to the research of [66], in the case of the intense presence of elemental carbon (C), the Organic Carbon accentuates the degree of absorption of the BC and thus increases the extent of solar energy attenuation available at the surface. In Figure 11, BCAOD550 (BC) is anticorrelated with SSAOD550 (SS) and SUAOD550 (SU) and DUAOD550 (DU) is anticorrelated with OMAOD550 (OM). In other words, in a BC-dominated environment like zones 1, 4, 5, 6, 7, and 8, for example, SU is weakly present in contrast to zones 2, 3, and 9 where the SU correlation value is higher than that of BC. Given to this, as aerosol types involved in this study can also be correlated with each other, it remains necessary to find not only individual effects but also combined effects of inputs variables on the predict one and according to zones.

However, according to [1, 3, 10, 11, 13, 18, 67, 68], aerosols contribute to the attenuation of incident radiation either by absorption or by diffusion. In addition, Sulphate and Sea Salt aerosols are excellent radiation scatters, while Dust, Black Carbon, and Organic Carbon aerosols are excellent absorbent (Black Carbon aerosols are ranked as the second most absorbent particle after CO2) [69, 70]. But, depending on the climatology of an area, the chemical composition of Organic Carbon can vary [71] and consequently their impact on the incident radiation. Making connection with the present work, from the coherence phase relations, all types of aerosols are negatively correlated with DNI and therefore contribute to attenuating the incident radiation as shown in [72]. In addition, the scattering aerosols (SU and SS) are in phase advance on DNI (arrows pointed upward), meaning that an increase in their concentration leads to DNI decrease (Figures 6 and 8, resp.). This result is in close agreement with those previously obtained in [18] Figure 4. On the other hand, absorbent aerosols (OM, BC, and DU) are in phase-delay on DNI (arrows pointed downward, see Figures 7, 9, and 10), meaning that an increase of DNI has a detrimental effect on these aerosols. This last relationship is due to the fact that when the hygroscopy of aerosols reduces, their influence on incident radiation also reduces [73].

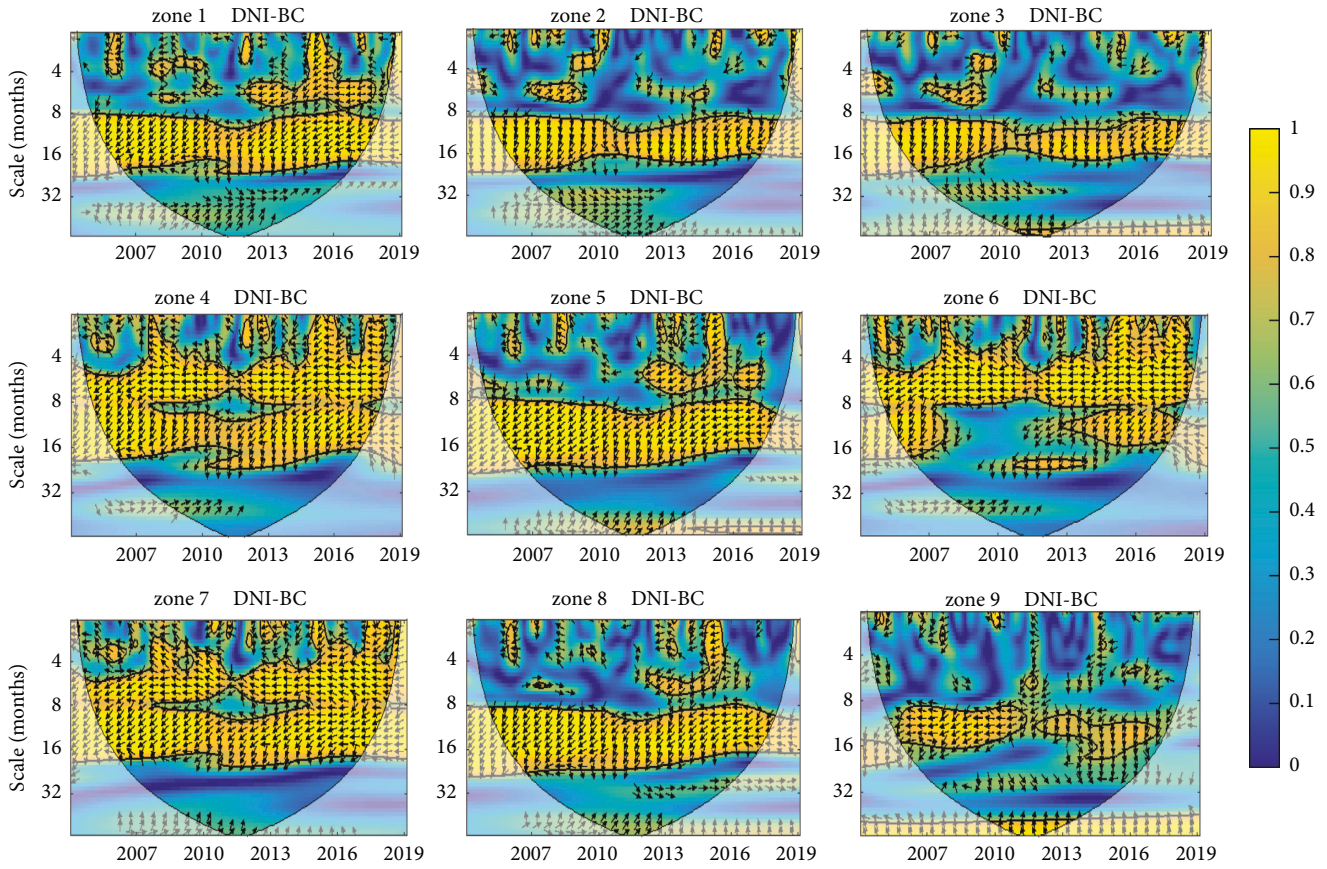

Figure 10: Wavelet coherence between the monthly average of DNI and BC time series (2005–2019). Areas of statistical significance are circled in black; the area outside the cone of influence has no statistical significance. The relative phase dependence is indicated by arrows (antiphase as oriented toward the left, and DNI in advance of phase to BC as arrows pointed downward).

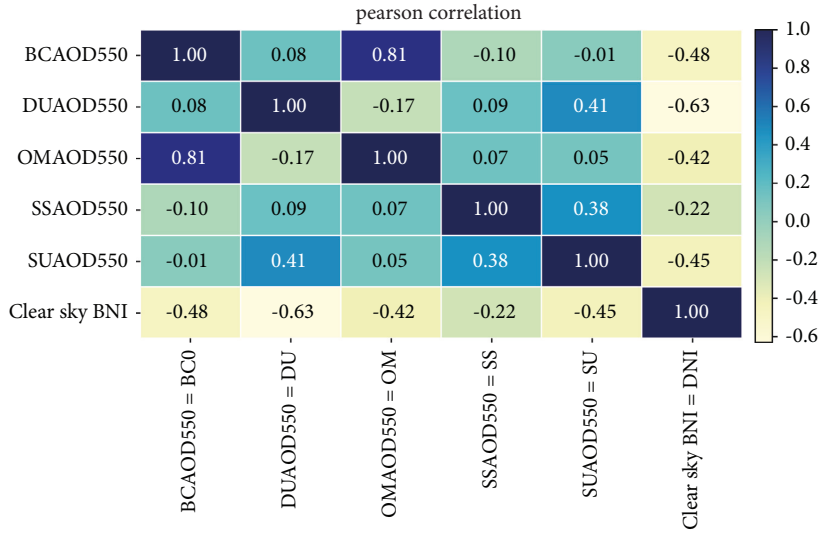

Figure 11: Pearson correlation matrix between five types of aerosols and Direct Normal Irradiation.

5. Conclusion

In this study, wavelet transformation analysis was applied to a 15-year (January 2005—December 2019) time series of different aerosol types and Direct Normal Irradiation collected in 9 zones throughout Cameroon. Through the spectral wavelet analysis of wavelet transform (CWS) and coherence wavelet transform (CWT), the time-frequency patterns of the analyzed data have been estimated as well as that of coherences between aerosols and DNI. Thus,

information about the dynamic behavior of the aerosol types, the DNI, and their connection with the DNI in each area over time was captured.

For the monthly average of all aerosol types, regardless of the zones, several frequencies have been identified in the CWS graphs, where the dominant frequency is at the 12-month period, since there is more wavelet power concentration within the 8–16-month band showing an annual frequency.

With the phase analysis, we found a negative relationship (arrows directed to the left) between DNI and all aerosol types (Desert Dust, Sea Salt, Sulfates, and Black and Organic Carbon), meaning that the increase of these aerosols negatively influences the amount of direct energy available. Conversely, the frequencies of correlation strongly depend on the aerosol types and the zones. We also found with the average wavelet coherence (AWC) and the percentage of significance coherence (PASC) that in almost all zones the Dust particles are the most correlated with the direct energy, showing the strong dependence of DNI on DU, and also that whenever OM is strongly correlated with DNI, BC is too (e.g., zone 7).With respect to the used methodology, the continuous wavelet transform method seems to be able to capture specific behaviors related to aerosols and direct energy exchange in each climate zone. This demonstrates the tool's suitability towards such study and, eventually, towards a meteorological field.

This analysis has significant potential for future research since, in addition to providing background information on the relationship between aerosols and direct energy, it also highlights the dynamical variation of such particles and thus may improve predictive solar energy models. Finally, the frequency patterns of aerosols in a given environment can serve as an indication of the soiling frequency of the solar collectors installed in that zone and also to explain the impact of some activities on the environment and the climate in general, since aerosols are partly coming from human activities.

Data Availability

Data come from free and open access data available in the following links: https://www.soda-pro.com/web-services/radiation/cams-radiation-service and https://www.soda-pro.com/web-services/atmosphere/\\cams-aod.

Disclosure

The views expressed herein do not necessarily represent those of UNESCO, IRDC, or its Board of Governors.

Conflicts of Interest

The authors declare that there are no conflicts of interest regarding the publication of this paper.

Authors' Contributions

Y. A. Douanla, O. Mamadou, and A. Dembélé determined the main objective of this study. O. Mamadou and A. Dembélé provided advice on data processing methods. Y. A. Douanla, D. R. Koukoui, and F. E. Akpoly analyzed the data and realized the results. Y. A. Douanla wrote the article with the contribution of all co-authors. O. Mamadou, A. Dembélé, and A. Lenouo contributed to the paper's content improvement and made suggestions on grammar and graphic formatting issues.

Acknowledgments

This work was carried out with the aid of a grant from UNESCO and the International Development Research Centre, Ottawa, Canada. The authors also thank SoDa, MERRA, and CAMS database administrators for providing open access to their databases. This research was funded by the German Academic Exchange Service (DAAD) section ST32 (Grant no. 57424259).

References

[1] O. Boucher, *Aérosols Atmosphériques: Propriétés et Impacts Climatiques*, Springer, Berlin, Germany, 2012.

[2] Z. Zhu, L. Lu, X. Yao, W. Zang, and W. Liu, *Ar6 Climate Change 2021: The Physical Science Basis*, International Plant Protection Convention, Rome, Italy, 2021.

[3] V. Ramanathan, P. J. Crutzen, J. T. Kiehl, and D. Rosenfeld, "Aerosols, climate, and the hydrological cycle," *Science*, vol. 294, no. 5549, pp. 2119–2124, 2001.

[4] N. Bellouin, O. Boucher, J. Haywood, and M. S. Reddy, "Global estimate of aerosol direct radiative forcing from satellite measurements," *Nature*, vol. 438, pp. 1138–1141, 2005.

[5] F. Solmon, N. Elguindi, M. Mallet, C. Flamant, and P. Formenti, "West African monsoon precipitation impacted by the south eastern atlantic biomass burning aerosol outflow," *NPJ Climate and Atmospheric Science*, vol. 4, no. 1, p. 54, 2021.

[6] Y. Balkanski, M. Schulz, T. Claquin, and S. Guibert, "Reevaluation of mineral aerosol radiative forcings suggests a better agreement with satellite and aeronet data," *Atmospheric Chemistry and Physics*, vol. 7, no. 1, pp. 81–95, 2007.

[7] H. Wang, G. Shi, S. Li, W. Li, B. Wang, and Y. Huang, "The impacts of optical properties on radiative forcing due to dust aerosol," *Advances in Atmospheric Sciences*, vol. 23, no. 3, pp. 431–441, 2006.

[8] J. Huang, C. Zhang, and J. M. Prospero, "Large-scale effect of aerosols on precipitation in the west african monsoon region," *Quarterly Journal of the Royal Meteorological Society*, vol. 135, no. 640, pp. 581–594, 2009.

[9] F. Solmon, M. Mallet, N. Elguindi, F. Giorgi, A. Zakey, and A. Konare, "Dust aerosol impact on regional precipitation over western africa, mechanisms and sensitivity to absorption properties," *Geophysical Research Letters*, vol. 35, no. 24, 2008.

[10] A. J. M. Komkoua, C. Tchawoua, D. A. Vondou, P. Choumbou, C. Kenfack Sadem, and S. Dey, "Impact of anthropogenic aerosols on climate variability over central africa by using a regional climate model," *International Journal of Climatology*, vol. 37, no. 1, pp. 249–267, 2017.

[11] A. J. M. Komkoua, G. M. Guenang, R. S. Tanessong, and A. Tchakoutio Sandjon, "Potential effects of aerosols on the diurnal cycle of precipitation over central africa by regcm4. 4," *SN Applied Sciences*, vol. 1, no. 2, 2019.

[12] O. Hodnebrog, G. Myhre, and B. H. Samset, "How shorter black carbon lifetime alters its climate effect," *Nature Communications*, vol. 5, no. 1, 2014.

[13] J. E. Penner, C. C. Chuang, and K. Grant, "Climate forcing by carbonaceous and sulfate aerosols," *Climate Dynamics*, vol. 14, no. 12, pp. 839–851, 1998.

[14] Y. Zhang, Y. J. Cai, F. Yu, G. Luo, and C. C. Chou, "Seasonal variations and long-term trend of mineral dust aerosols over the taiwan region," *Aerosol and Air Quality Research*, vol. 21, no. 5, Article ID 200433, 2021.

[15] F. Paulot, D. Paynter, M. Winton et al., "Revisiting the impact of sea salt on climate sensitivity," *Geophysical Research Letters*, vol. 47, no. 3, Article ID e2019GL085601, 2020.

[16] M. Schaper, "Direct normal irradiation," 2017, https://wiki.openmod-initiative.org/wiki/Direct_Normal_Irradiation.

[17] P. Blanc, B. Espinar, N. Geuder et al., "Direct normal irradiance related definitions and applications: the circumsolar issue," *Solar Energy*, vol. 110, pp. 561–577, 2014.

[18] Y. Douanla Alotse, A. Dembélé, O. Mamadou, and A. Lenouo, "Prediction of daily direct solar energy based on xgboost in Cameroon and key parameter impacts analysis," in *Proceedings of the 2022 IEEE Multi-conference on Natural and Engineering Sciences for Sahel's Sustainable Development (MNE3SD)*, IEEE, Ouagadougou, Burkina Faso, February 2022.

[19] E. Foufoula-Georgiou and P. Kumar, "Wavelet analysis in geophysics: an introduction," in *Wavelet Analysis and its Applications*Elsevier, Amsterdam, Netherlands, 1994.

[20] E. Foufoula-Georgiou and P. Kumar, "Wavelet analysis in geophysics: an introduction," *Wavelets in geophysics*, vol. 4, pp. 1–43, 1994.

[21] D. T. L. Lee and A. Yamamoto, "Wavelet analysis: theory and applications," *Hewlett-Packard Journal*, vol. 45, p. 44, 1994.

[22] C. Torrence and G. P. Compo, "A practical guide to wavelet analysis," *Bulletin of the American Meteorological Society*, vol. 79, no. 1, pp. 61–78, 1998.

[23] S. Pal and P. Devara, "A wavelet-based spectral analysis of long-term time series of optical properties of aerosols obtained by lidar and radiometer measurements over an urban station in western India," *Journal of Atmospheric and Solar-Terrestrial Physics*, vol. 84, pp. 75–87, 2012.

[24] N. Palizdan, Y. Falamarzi, Y. F. Huang, and T. S. Lee, "Precipitation trend analysis using discrete wavelet transform at the langat river basin, selangor, Malaysia," *Stochastic Environmental Research and Risk Assessment*, vol. 31, no. 4, pp. 853–877, 2017.

[25] J. Adepitan and E. Falayi, "Variability changes of some climatology parameters of Nigeria using wavelet analysis," *Scientific African*, vol. 2, Article ID e00017, 2019.

[26] Q. Li, P. He, Y. He et al., "Investigation to the relation between meteorological drought and hydrological drought in the upper shaying river basin using wavelet analysis," *Atmospheric Research*, vol. 234, Article ID 104743, 2020.

[27] G. Vivone, G. D'Amico, D. Summa et al., "Atmospheric boundary layer height estimation from aerosol lidar: a new approach based on morphological image processing techniques," *Atmospheric Chemistry and Physics*, vol. 21, no. 6, pp. 4249–4265, 2021.

[28] Y. Zhu, J. Liao, W. Gong et al., "Air pollutants sources in winter in chang-zhu-tan region of China," *Advances in Meteorology*, vol. 2022, Article ID 9717192, 9 pages, 2022.

[29] G. Barik, P. Acharya, A. Maiti et al., "A synergy of linear model and wavelet analysis towards space-time characterization of aerosol optical depth (aod) during pre-monsoon season (2007–2016) over indian sub-continent," *Journal of Atmospheric and Solar-Terrestrial Physics*, vol. 211, Article ID 105478, 2020.

[30] M. Conte, D. Contini, and A. Held, "Multiresolution decomposition and wavelet analysis of urban aerosol fluxes in Italy and Austria," *Atmospheric Research*, vol. 248, Article ID 105267, 2021.

[31] Y. Meng and W. Sun, "Relationship between the formation of pm2.5 and meteorological factors in northern China: the periodic characteristics of wavelet analysis," *Advances in Meteorology*, vol. 2021, Article ID 9723676, 14 pages, 2021.

[32] R. C. Deo, X. Wen, and F. Qi, "A wavelet-coupled support vector machine model for forecasting global incident solar radiation using limited meteorological dataset," *Applied Energy*, vol. 168, pp. 568–593, 2016.

[33] C. Xu, "Detecting periodic oscillations in astronomy data: revisiting wavelet analysis with coloured and white noise," *Monthly Notices of the Royal Astronomical Society*, vol. 466, no. 4, pp. 3827–3833, 2017.

[34] T. Zhu, H. Wei, X. Zhao, C. Zhang, and K. Zhang, "Clear-sky model for wavelet forecast of direct normal irradiance," *Renewable Energy*, vol. 104, 2017.

[35] T. P. Chang, F. J. Liu, H. H. Ko, and M. C. Huang, "Oscillation characteristic study of wind speed, global solar radiation and air temperature using wavelet analysis," *Applied Energy*, vol. 190, pp. 650–657, 2017.

[36] F. Li and L. He, "The effects of dominant driving forces on summer precipitation during different periods in Beijing," *Atmosphere*, vol. 8, no. 12, 2017.

[37] Z. Li, J. Yue, Y. Xiang et al., "Multiresolution analysis of the relationship of solar activity, global temperatures, and global warming," *Advances in Meteorology*, vol. 2018, Article ID 2078057, 8 pages, 2018.

[38] M. Tingem, M. Rivington, and J. Colls, "Climate variability and maize production in Cameroon: simulating the effects of extreme dry and wet years," *Singapore Journal of Tropical Geography*, vol. 29, no. 3, pp. 357–370, 2008.

[39] T. E. Epule, A. Chehbouni, D. Dhiba et al., "Vulnerability of maize, millet, and rice yields to growing season precipitation and socio-economic proxies in Cameroon," *PLoS One*, vol. 16, no. 6, Article ID e0252335, 2021.

[40] D. François, Y. Gautier, and G. Emmanuelle, "Milieu equatorial, le climat-encyclopædia universalis," 2015, https://www.universalis.fr/encyclopedie/milieu-equatorial/1-le-climate.

[41] M. D. C. Tongco, "Purposive sampling as a tool for informant selection," *Ethnobotany Research and Applications*, vol. 5, pp. 147–158, 2007.

[42] Z. Van Arkel and A. L. Kaleita, "Identifying sampling locations for field-scale soil moisture estimation using *k*-means clustering," *Water Resources Research*, vol. 50, no. 8, pp. 7050–7057, 2014.

[43] H. Taherdoost, "Sampling methods in research methodology; how to choose a sampling technique for research," *How to Choose a Sampling Technique for Research*, vol. 5, 2016.

[44] X. Zhang, Y. He, Y. Jin, H. Qin, M. Azhar, and J. Z. Huang, "A robust *k*-means clustering algorithm based on observation point mechanism," *Complexity*, vol. 2020, Article ID 3650926, 11 pages, 2020.

[45] R. Nainggolan, R. Perangin-angin, E. Simarmata, and A. F. Tarigan, "Improved the performance of the k-means cluster using the sum of squared error (sse) optimized by using the elbow method," *Journal of Physics: Conference Series*, vol. 1361, 2019.

[46] F. Wang, H. Franco-Penya, J. D. Kelleher, J. Pugh, and R. Ross, "An analysis of the application of simplified silhouette to the evaluation of k-means clustering validity," in *Proceedings of the International Conference on Machine Learning*

and Data Mining in Pattern Recognition, pp. 291–305, Springer, Berlin, Germany, July 2017.

[47] M. Syakur, B. Khotimah, E. Rochman, and B. D. Satoto, "Integration *K*-means clustering method and elbow method for identification of the best customer profile cluster," *IOP Conference Series: Materials Science and Engineering*, vol. 336, 2018.

[48] S. Nanjundan, S. Sankaran, C. Arjun, and G. P. Anand, "Identifying the number of clusters for *K*-means: a hypersphere density based approach," 2019, https://arxiv.org/ftp/arxiv/papers/1912/1912.00643.pdf.

[49] C. S. Schuster, "The quest for the optimum angular-tilt of terrestrial solar panels or their angle-resolved annual insolation," *Renewable Energy*, vol. 152, pp. 1186–1191, 2020.

[50] A. Beyoud, N. Hassanain, and A. Bouhaouss, "Correlation between diffuse solar irradiation and linke turbidity factor in Rabat, (Morocco)," *IOSR Journal of Applied Physics*, vol. 12, 2020.

[51] P. S. Addison, "Introduction to redundancy rules: the continuous wavelet transform comes of age," *Philosophical Transactions of The Royal Society A Mathematical Physical and Engineering Sciences*, vol. 376, 2018.

[52] J. B. Tary, R. H. Herrera, and M. van der Baan, "Analysis of time-varying signals using continuous wavelet and synchrosqueezed transforms," *Philosophical Transactions of the Royal Society A: Mathematical, Physical & Engineering Sciences*, vol. 376, no. 2126, Article ID 20170254, 2018.

[53] F. Anctil and G. Pelletier, "Analyse en ondelettes de fluctuations de débit en réseau de distribution d'eau potable," *Revue des sciences de l'eau/Journal of Water Science*, vol. 24, no. 1, pp. 25–33, 2011.

[54] C. Damerval, "Ondelettes pour la détection de caractéristiques en traitement d'images, application à la détection de région d'intérêt. mathématiques [math]," B.Sc. thesis, Université Joseph-Fourier-Grenoble I, France, 2008.

[55] J. Bitton, "Analyse multi-échelle de l'évolution des flux de chaleur sensible et latente échangés entre un écosystème forestier et l'atmosphère au moyen de la transformée en ondelettes continue," M.Sc. thesis, Gembloux Agro-Bio Tech, Gembloux, Belgium, 2019.

[56] T. Abid, "Analyse du signal ECG par les ondelettes," 2008, https://biblio.univ-annaba.dz/wp-content/uploads/2014/05/Memoire-du-Magistere_-ABID-Tarek.pdf.

[57] S. Jemai, M. Ellouze, and H. Abida, "Variability of precipitation in arid climates using the wavelet approach: case study of watershed of gabes in south-east Tunisia," *Atmosphere*, vol. 8, no. 9, 2017.

[58] A. Grinsted, J. C. Moore, and S. Jevrejeva, "Application of the cross wavelet transform and wavelet coherence to geophysical time series," *Nonlinear Processes in Geophysics*, vol. 11, pp. 561–566, 2004.

[59] H. Wei, "Matlab code for multiple wavelet coherence and partial wavelet coherency," 2020, https://figshare.com/articles/software/Matlab_code_for_multiple_wavelet_coherence_and_partial_wavelet_coherency/13031123/2.

[60] D. Nalley, J. Adamowski, A. Biswas, B. Gharabaghi, and W. Hu, "A multiscale and multivariate analysis of precipitation and streamflow variability in relation to enso, nao and pdo," *Journal of Hydrology*, vol. 574, pp. 288–307, 2019.

[61] J. Maley, "Dust, clouds, rain types, and climatic variations in tropical north Africa," *Quaternary Research*, vol. 18, 1982.

[62] R. T. Loua, H. Bencherif, N. Mbatha et al., "Study on temporal variations of surface temperature and rainfall at conakry airport, Guinea: 1960–2016," *Climate*, vol. 7, no. 7, 2019.

[63] C. Andronache, "Wet removal of atomospheric particles by rain," *Acid Rain Research Focus*, Nova, Nagoya, Japan, 2008.

[64] H. L. Aboubacar, *Analyse socio-économique de la filière artisanale d'huile de palme dans la région de la sanaga-maritime (Cameroun)*, Ph.D. thesis, CIHEAM, Zaragoza, Spain, 2013.

[65] M. N. Essam, "Sanaga maritime," 2021, https://www.sanaga-maritime-info.com/wp-content/uploads/2021/07/Sanaga-Maritime-Info-Avril-2021.pdf.

[66] Y. Han, J. Cao, J. Chow, J. Watson, Z. An, and S. Liu, "Elemental carbon in urban soils and road dusts in xi'an, China and its implication for air pollution," *Atmospheric Environment*, vol. 43, no. 15, pp. 2464–2470, 2009.

[67] K. M. Latha and K. Badarinath, "Spectral solar attenuation due to aerosol loading over an urban area in India," *Atmospheric Research*, vol. 75, no. 4, pp. 257–266, 2005.

[68] K. Papachristopoulou, I. Fountoulakis, A. Gkikas et al., "15-year analysis of direct effects of total and dust aerosols in solar radiation/energy over the mediterranean basin," *Remote Sensing*, vol. 14, no. 7, p. 1535, 2022.

[69] V. Adam, "Aerosols: tiny particles, big impact," 2020, https://earthobservatory.nasa.gov/features/Aerosols.

[70] I. Coll, "Connaissances sur les enjeux environnementaux et climatiques des particules," *Pollution atmosphérique. Climat, santé, société*, 2012.

[71] T. W. Kirchstetter and T. L. Thatcher, "Contribution of organic carbon to wood smoke particulate matter absorption of solar radiation," *Atmospheric Chemistry and Physics*, vol. 12, no. 14, pp. 6067–6072, 2012.

[72] W. Meesang, S. Bualert, A. Tremper, N. Kitwiroon, and M. Pirani, "Influence of concentrations dried sea salt aerosols to decrease solar radiation," *Modern Applied Science*, vol. 9, no. 1, 2014.

[73] Y. Wei, Q. Zhang, and J. Thompson, "Atmospheric black carbon can exhibit enhanced light absorption at high relative humidity," *Atmospheric Chemistry and Physics Discussions*, vol. 13, no. 11, 2013.